Parametric study on thermal and hydraulic characteristics of laminar flow in microchannel heat sink with fan-shaped ribs on sidewalls – Part 3: performance evaluation

Lei Chai[a, *], Guo Dong Xia[b], Hua Sheng Wang[a]

[a] School of Engineering and Materials Science, Queen Mary University of London, Mile End Road, London E1 4NS, UK

[b] Key Laboratory of Enhanced Heat Transfer and Energy Conservation, Ministry of Education, College of Environmental and Energy Engineering, Beijing University of Technology, Beijing, China

Abstract   In order to comprehensively assess the performance of microchannel heat sink with fan-shaped ribs on sidewalls, this third part of a three-part study focuses on the relationship between thermal resistance and pumping power, and further the entropy generation rate and performance evaluation criteria, with water and silicon used as fluid and solid for the computational domain. The microchannel has the width of 0.1 mm and depth of 0.2 mm in the constant cross-section region. The geometric parameters include the width (0.005-0.4 mm), height (0.005-0.025 mm) and spacing (0.2-5 mm) of aligned or offset fan-shaped ribs. For deep insight into the basic mechanisms and properties of such heat sinks, the entropy generation rate due to heat transfer and fluid friction are separately studied. Results show that the fan-shaped ribs can lead to better comprehensive performance and the geometric parameters of fan-shaped ribs have a significant influence on the performance of such microchannel heat sinks. With the increase of the rib's height, the microchannel heat

---

[*] Corresponding author. Tel.: +44 20 7882 7306.

E-mail address: l.chai@qmul.ac.uk (Lei Chai).

sinks with offset fan-shaped ribs gradually perform better than the ones with aligned fan-shaped ribs. With the decrease of the rib's spacing, the comprehensive performance firstly becomes better and then gradually deteriorates. For the microchannel heat sink with large rib's height and small rib's spacing, the increase of Reynolds number can lead to tremendously increase of entropy generation rate due to fluid friction, which can withdraw the decrease of entropy generation rate due to heat transfer and lead to the increase of total entropy generation rate, making the comprehensive performance worse than the smooth one. For Reynolds number ranging from 187 to 715 and studied geometric parameters, the best microchannel heat sink shows a 32% decrease in entropy generation rate and 1.33 in performance evaluation criterion, comparing with the smooth one.

Key words   microchannel heat sink; fan-shaped ribs; entropy generation rate; performance evaluation criterion

1. Introduction

With the development of microelectromechanical devices, the microchannel heat sink has been successfully used for heat removal in a variety of devices, such as micropumps, microvalves, and microsensors. Further, the higher volumetric heat transfer densities require advanced manufacturing techniques and lead to more complex manifold designs. Recently, a significant amount of research work has been developed as innovative cooling techniques those have the potential to deliver high-heat flux rates for microelectronic applications [1]. Xu et al. [2, 3] used the thermal boundary layer redeveloping concept to demonstrate the

interrupted microchannel heat sink to improve the heat transfer performance. Chai et al. [4, 5] took advantage of the interruption of boundary layer formation and establishment of secondary flow to develop the microchannel heat sinks with periodic expansion-constriction cross-sections. Cheng [6], Hong and Cheng [7] and Foong et al. [8] based on the enhanced mixing mechanism of cold and hot fluids to introduce the passive microstructures into the microchannels. Combining the advantages of interrupted microchannel and passive microstructures, Chai et al. [9] introduced the staggered rectangular ribs into the transverse microchambers for better heat transfer performance.

However, employing microchannel heat sink usually results in a higher pressure drop per unit length, although with higher heat transfer performance. Therefore, the application of microchannels to electronics cooling imposes severe design constraints on the system design. For a given heat dissipation rate, the flow rate, pressure drop, fluid temperature rise, and fluid inlet to surface temperature difference requirements necessitate optimization of the channel geometry [10]. For the optimization design of microchannel heat sink, several experimental, numerical and theoretical studies on the optimization of microchannel heat sinks have been conducted. Tsai and Reiyu [11] and Liu and Garimella [12] established theoretical optimization models based on thermal resistance minimization for a given pumping power to predict microchannel heat sink performance. Singhal et al. [13], Kandlikar and Upadhye [14], Gosselin and Bejan [15], and Canhoto and Reis [16] carried out optimization methods based on the minimization of pumping power requirement for a given thermal resistance to evaluate the heat transfer performance. For further study the optimization of thermal and hydraulic resistances simultaneously with all relevant design parameters for microchannel heat sinks

including geometric parameters, material properties and flow conditions, Xie et al. [17] used the relationship between the thermal resistance and the pumping power to evaluate the heat transfer enhancement performance of the microchannel heat sinks with internal vertical Y-shaped bifurcations. Famouri et al. [18] and Shi and Dong [19] applied optimization methods based on entropy generation minimization for the optimization of a variable-height shrouded fin array and microchannel with staggered arrays of pin fin structure, respectively. Promvonge et al. [20], Xia et al. [21, 22], Chai et al. [9], and Zhang et al. [23] used the performance evaluation criteria to comprehensively access the heat transfer enhancement performance of microchannel heat sinks with passive microstructures.

In the first and second parts of this three-part study, three-dimensional numerical models have been carried out to examine the laminar flow and heat transfer characteristics in the microchannel heat sink with fan-shaped ribs on sidewalls. To study the effects of geometric parameters of fan-shaped ribs on thermal and hydraulic characteristics, three non-dimensional variables have been designed, respectively representing the width, height and spacing of aligned and offset fan-shaped ribs. In order to comprehensively assess the performance of such microchannel heat sink, this part of the study is to focus on the relationship between thermal resistance and pumping power, entropy generation rate and performance evaluation criteria for laminar flow in such microchannel heat sink with the purpose of optimum channel geometric configuration.

2. Model formulation and solution methodology

Figure 1a illustrates schematic of the enhanced microchannel heat sink, which also used as the computational domain. In this design, the fan-shaped ribs are mounted on the two

parallel sidewalls in tandem for both aligned and offset arrangements. The computational

domain has the length of 10 mm, width of 0.25 mm, and height of 0.35 mm. The

microchannel has the length of 10 mm and the depth of 0.2 mm, respectively. The width of

the two parallel sidewalls for microchannel without ribs (W_c) is 0.1 mm. The geometric

parameters of fan-shaped ribs studied in this paper are shown in Fig. 1b, including the width

(W_r), the height (H_r), and the spacing (S_r). The ranges for these geometric parameters

examined in this paper are 0.005-0.4 mm for W_r, 0.005-0.025 mm for H_r, and 0.2-5 mm for S_r.

Three non-dimensional variables are designed to analyze their effects on thermal and

hydraulic characteristics, including the ratio of the width of rib to the spacing (W_r/S_r), the ratio

of the height of rib to the width of the two parallel sidewalls (H_r/W_c), and the ratio of the

spacing of ribs to the width of the two parallel sidewalls (S_r/W_c), respectively.

The simulations are performed using the ANSYS FLUENT 12.0 software. The

SIMPLEC algorithm is applied to solve the governing differential equations for the velocity,

pressure and temperature fields in the microchannels. These governing equations are listed as

follows:

$$\frac{\partial}{\partial x_i}\left(\rho u_i\right)=0 \tag{1}$$

$$\frac{\partial}{\partial x_i}\left(\rho_f u_i u_j\right)=-\frac{\partial p}{\partial x_j}+\frac{\partial}{\partial x_i}\left[\mu_f\left(\frac{\partial u_j}{\partial x_i}+\frac{\partial u_i}{\partial x_j}\right)\right] \tag{2}$$

$$\frac{\partial}{\partial x_i}\left(\rho_f u_i c_{pf} T\right)=\frac{\partial}{\partial x_i}\left(k_f\frac{\partial T}{\partial x_i}\right)+\mu_f\left[2\left(\frac{\partial u_i}{\partial x_i}\right)^2+\left(\frac{\partial u_j}{\partial x_i}+\frac{\partial u_i}{\partial x_j}\right)^2\right] \tag{3}$$

For the solid

$$\frac{\partial}{\partial x_i}\left(k_s\frac{\partial T}{\partial x_i}\right)=0 \tag{4}$$

where ρ is density, μ is dynamic viscosity, c_p is specific heat capacity, k is thermal

conductivity, x_1, x_2 and x_3 are x, y and z coordinates, respectively, as shown in Fig. 1a. Subscripts f and s refer to fluid and solid, respectively.

At the channel inlet and outlet, the velocity-inlet and pressure-outlet boundaries are applied. The solid part of the heat sink corresponding to the inlet and outlet of the channel is maintained as an adiabatic boundary. At the interior walls of the channel, no-slip and no-penetration boundary conditions are applied. At the base of heat sink, constant heat flux boundary condition is used. At the top surface of the computational domain including solid and fluid, an adiabatic boundary is assumed. Due to symmetry of the problem, symmetry boundary is maintained at the two sides of the computational domain. The parameters used in this study are in the following ranges: the velocity-inlet u_{in} are selected as the average velocity in the constant cross-section region $\bar{u}$ = 1, 2, 3, 4 and 5 m·s^{-1}, the temperature at the channel inlet T_{in} = 293 K, the pressure at the channel outlet p_{out} = 0 (gauge pressure) and constant heat flux at the heat sink base q_w = 10^6 W·m^{-2}. The fluid and solid are water and silicon, respectively. The thermo-physical properties of water including ρ_f, μ_f, c_{pf} and k_f depend on temperatures in accordance to Incropera [24]. The thermal conductivity of silicon k_s is set as a constant of 148 W·m^{-1} K^{-1} in the computations.

The solutions are considered to be converged when the normalized residual values are less than 10^{-5} for all the variables. For every microchannel heat sink, a grid independence test is conducted using several different mesh sizes. The grid independence test and the physical model validation test are similar to Chai et al. [25].

3. Data acquisition

Loosen [26] proposed a simplified one-dimensional analytical model to study the thermal resistance. The total thermal resistance of microchannel heat sink is defined as

$$R_{th} = \frac{\overline{T_w} - T_{in}}{q_w LW} \tag{5}$$

where q_w is the heat flux at the silicon base, L and W are respectively the length and width of silicon base, T_{in} is the water temperature in the channel inlet, $\overline{T_w}$ is the area-weighted temperature of the silicon base and defined as

$$\overline{T_w} = \frac{\int T_{w,x,y}\, dy dx}{\int dy dx} \tag{6}$$

The pumping power are defined as

$$P_p = \Delta p_{mic}\, \overset{g}{V} \tag{7}$$

where $\overset{g}{V}$ is the fluid volume flow rate, Δp_{mic} is the pressure drop of the microchannel ($\Delta p_{mic} = p_{in} - p_{out}$), p_{in} is the mass-weighted average pressure and defined as

$$p_{in} = \frac{\int p_{in,i}\, \rho_{f,i} \left| \overset{r}{u} \cdot \overset{r}{dA} \right|}{\int \rho_{f,i} \left| \overset{r}{u} \cdot \overset{r}{dA} \right|} \tag{8}$$

Khan et al. [27] proposed an entropy generation minimization procedure to optimize the overall performance of microchannel heat sinks. This procedure allowed the combined effect of thermal resistance and pressure drop to be assessed simultaneously as the heat sink interacts with the surrounding flow field.

$$S_{gen} = S_{gen,h} + S_{gen,f} = \frac{Q(\overline{T_w} - T_a)}{T_w T_a} + \frac{\overset{g}{m}(p_{in} - p_{out})}{\rho_f T_a} \tag{9}$$

where Q is the heat transfer rate, ρ_f is the volume average fluid density, T_a is the ambient temperature and assumed to $T_a = T_{in}$, $\overset{g}{m}$ is the fluid mass flow rate, S_{gen} is the total entropy generation rate, and $S_{gen,h}$ and $S_{gen,f}$ are the entropy generation rates due to heat transfer and

fluid friction, respectively.

In order to access the enhanced heat transfer surfaces in heat exchanger design, Webb [28] outlined detailed procedures to calculate the performance improvement and to select the optimum surface geometry. For the microchannel heat sink with offset ribs on sidewalls, the performance evaluation criteria (PEC) is defined as the ratio of the heat transfer coefficient ($\bar{h}$) to the smooth microchannel heat sink ($\bar{h}_0$) at an equal pumping power. For a constant pumping power,

$$(\dot{V}\,\Delta p)_0 = (\dot{V}\,\Delta p) \tag{10}$$

The relationship between the average friction factor and Reynolds number can be expressed as

$$f_{ave,0}Re_0^3 = f_{ave}Re^3 \tag{11}$$

$$Re_0 = Re(f_{ave} / f_{ave,0})^{1/3} \tag{12}$$

Therefore, the PEC is given by

$$PEC = \frac{\bar{h}}{h_0}\Big|_{pp} = \frac{\overline{Nu}}{\overline{Nu_0}}\Big|_{pp} = \frac{\overline{Nu}/\overline{Nu_0}}{(\bar{f}/\bar{f}_0)^{1/3}} \tag{13}$$

where $\overline{Nu_0}$ and $\bar{f}_0$ respectively stand for Nusselt number and friction factor of the smooth microchannel heat sink. The average Fanning friction factor is given by

$$\bar{f} = \frac{(p_{in} - p_{out})D_h}{2\rho_f L\bar{u}^2} \tag{14}$$

where D_h is the hydraulic diameter calculated based on the constant cross-section region. The average heat transfer coefficient and Nusselt number are given by

$$\bar{h} = \frac{q_w LW}{A(\overline{T_w} - \overline{T_f})} \tag{15}$$

8

$$\overline{Nu} = \frac{\overline{h}D_{\mathrm{h}}}{k_{\mathrm{f}}} \qquad (16)$$

where A is the inner wall/ fluid contact surface area based on the smooth microchannel, k_{f} is

the mass-average fluid thermal conductivity. The Reynolds number are defined as

$$Re = \frac{\rho_{\mathrm{f}}\overline{u}D_{\mathrm{h}}}{\mu_{\mathrm{f}}} \qquad (17)$$

where μ_{f} is the mass-average fluid dynamic viscosity.

4. Results and discussion

4.1. Thermal resistance and pumping power

Figure 2 shows the effect of $W_{\mathrm{r}}/S_{\mathrm{r}}$ on the relationship between R_{th} and P_{p} with Re = 187,

316, 443, 582 and 715. The solid black line is for the smooth microchannel heat sink (MCHS).

The geometry of fan-shaped ribs used in this figure is W_{c} = 0.1 mm, H_{r} = 0.025 mm, S_{r} = 0.4

mm and W_{r} = 0.1, 0.2, 0.3 and 0.4 mm. It is noticed that the R_{th} drops quickly with increase of

P_{p} for all the microchannel heat sinks, due to the increase of heat transfer coefficient and the

decrease of average fluid temperature with increase of P_{p} [4]. It can be observed that the

microchannel heat sink with fan-shaped ribs leads to lower R_{th} at the same P_{p}, indicating the

better comprehensive performance. For $W_{\mathrm{r}}/S_{\mathrm{r}}$ = 0.25 and 0.5, the microchannel heat sink with

offset fan-shaped ribs (MCHS-OFR) has obviously better performance than the one with

aligned fan-shaped ribs (MCHS-AFR), while for $W_{\mathrm{r}}/S_{\mathrm{r}}$ = 0.75 and 1, the MCHS-OFR shows

just a little better than MCHS-AFR.

Figure 3 shows the effect of $H_{\mathrm{r}}/W_{\mathrm{c}}$ on the relationship between R_{th} and P_{p} with Re = 187,

316, 443, 582 and 715. The geometry of fan-shaped ribs used in this figure is W_{c} = 0.1 mm, S_{r}

= 0.4 mm, W_{r} = 0.1 mm and H_{r} = 0.005, 0.015 and 0.025 mm. It can be found that the

MCHS-OFR with $H_r/W_c = 0.15$ shows much better performance than that with $H_r/W_c = 0.05$, and just a little worse than that with $H_r/W_c = 0.25$; The MCHS-AFR with $H_r/W_c = 0.15$ shows the better heat transfer performance than those with $H_r/W_c = 0.05$ and 0.25. It is also noted that the MCHS-AFR has better performance than MCHS-OFR for $H_r/W_c = 0.05$, while the contrary tendency for $H_r/W_c = 0.15$ and 0.25. It is also seen that with the increase of H_r, the P_p extremely increases for MCHS-AFR due to the large increase of pressure drop.

Figure 4 shows the effect of S_r/W_c on the relationship between R_{th} and P_p with $Re = 187$, 316, 443, 582 and 715. The geometry of fan-shaped ribs used in this figure is $W_c = 0.1$ mm, $W_r = 0.1$ mm, $H_r = 0.025$ mm and $S_r = 0.25, 0.5, 1$ and 2 mm. It is noted that the MCHS-AFR with $S_r/W_c = 10$ and 5 have a little better performance than those with $S_r/W_c = 20$ and 2.5, while the MCHS-OFR with $S_r/W_c = 5$ and 2.5 perform better than those with $S_r/W_c = 20$ and 10, suggesting that there are a range of S_r for better performance. From Figs. 2, 3 and 4, it also can be observed that the relationship between R_{th} and P_p is not very clear to present the comprehensive thermal performance if the heat sink has many changed geometric parameters, because the R_{th} and P_p separately present the performance of heat transfer and pressure drop.

4.2. Entropy generation rate

Figures 5a, 5b and 5c respectively show the effects of W_r/S_r on S_{gen}, $S_{gen,h}$ and $S_{gen,f}$ with $Re = 187$, 316, 443, 582 and 715. The geometry of fan-shaped ribs used in these figures is the same as Fig. 2. It can be noted that the fan-shaped ribs can result in lower S_{gen} and $S_{gen,h}$, but higher $S_{gen,f}$. From Fig. 5b, it is noticed that the increase of Re leads to obvious decreases of $S_{gen,h}$, there is no much difference of $S_{gen,h}$ between MCHS-OFR and MCHS-AFR, and the

10

W_r/S_r does not have obvious influence on $S_{\mathrm{gen,h}}$. From Fig. 5c, it can be seen that the quantity of $S_{\mathrm{gen,f}}$ is largely lower than $S_{\mathrm{gen,h}}$, but tremendously increases with increase of Re, and the increase rate is much higher than MCHS, further the MCHS-AFR shows larger increase rate than MCHS-OFR. With the increase of Re, the $S_{\mathrm{gen,f}}$ can have an significant influence on S_{gen}. The increase of W_r/S_r and Re leads to much larger $S_{\mathrm{gen,f}}$, which can withdraw the deceased $S_{\mathrm{gen,h}}$ and result in deterioration of such heat sink performance. As shown in Fig. 5a, under the influence of both $S_{\mathrm{gen,h}}$ and $S_{\mathrm{gen,f}}$, the S_{gen} decreases with increase of Re as $Re < 443$, while the decrease rate becomes lower or even minus with increase of Re as $Re > 443$.

Figures 6a, 6b and 6c respectively show the effect of H_r/W_c on S_{gen}, $S_{\mathrm{gen,h}}$ and $S_{\mathrm{gen,f}}$ with $Re = 187, 316, 443, 582$ and 715. The geometry of fan-shaped ribs used in these figures is the same as Fig. 3. From Fig. 6a, it can be seen that the increase of H_r/W_c leads to large decrease of S_{gen}, except the MCHS-AFR with $H_r/W_c = 0.25$ as $Re > 582$. As $H_r/W_c = 0.05$ and 0.15, S_{gen} of MCHS-AFR is a litter lower than MCHS-OFR, while as $H_r/W_c = 0.25$, they show almost the same S_{gen} as $Re < 443$ and the MCHS-AFR is evidently larger than MCHS-OFR as $Re > 443$. From Figs. 6b and 6c, it can be seen that the increase of H_r/W_c results in large decrease of $S_{\mathrm{gen,h}}$ and extreme increase of $S_{\mathrm{gen,f}}$ for both MCHS-AFR and MCHS-OFR. Further with the increase of H_r/W_c, the MCHS-AFR shows almost the same $S_{\mathrm{gen,h}}$ but much higher $S_{\mathrm{gen,f}}$ than MCHS-OFR. Especially for MCHS-AFR with $H_r/W_c = 0.25$ as $Re > 582$, the increase of $S_{\mathrm{gen,f}}$ withdraws the decrease of $S_{\mathrm{gen,h}}$, leading to the increase of S_{gen} with Re as shown in Fig. 6a.

Figures 7a, 7b and 7c respectively show the effect of S_r/W_c on S_{gen}, $S_{\mathrm{gen,h}}$ and $S_{\mathrm{gen,f}}$ with $Re = 187, 316, 443, 582$ and 715. The geometry of fan-shaped ribs used in these figures is the same as Fig. 4. From Fig. 7a, it can be seen that the decrease of S_r/W_c generally leads to

decrease of S_{gen}, except the MCHS-AFR with S_r/W_c = 5 and 2.5 as Re > 443 and MCHS-OFR

with S_r/W_c = 2.5 as Re > 582. From Fig. 7b, it can be found that the decrease of S_r/W_c

generally leads to obvious decrease of $S_{gen,h}$ and there is no much difference of $S_{gen,h}$ between

MCHS-AFR and MCHS-OFR. From Fig. 7c, it is noticed that with the increase of Re, the

increase of S_r/W_c results in extreme increase of $S_{gen,f}$, and the MCHS-AFR shows higher $S_{gen,f}$

than MCHS-OFR. As shown in Fig. 7a, the MCHS-AFR with S_r/W_c = 5 and 2.5 as Re > 443

and MCHS-OFR with S_r/W_c = 2.5 as Re > 582, the increase of $S_{gen,f}$ withdraws the decrease of

$S_{gen,h}$, leading to the increase of S_{gen} with Re.

To further investigate the influence of the channel geometric configuration on entropy

generation rate, Fig. 8a shows the effects of W_r/S_r and Re on the entropy generation rate ratio

to the MCHS ($S_{gen}/S_{gen,0}$), and Fig. 8b shows the effects of W_r/S_r and Re on the entropy

generation rate ratio due to heat transfer ($S_{gen,h}/S_{gen}$). The geometry of fan-shaped ribs used in

these figures is W_c = 0.1 mm, H_r = 0.025 mm, S_r = 0.4 mm and W_r = 0.05-0.4 mm. From Fig.

8a, it can be seen that there is no very clear relationship between W_r/S_r and $S_{gen}/S_{gen,0}$. For

MCHS-AFR, the $S_{gen}/S_{gen,0}$ for Re = 187 and 316 generally decreases with W_r/S_r as W_r/S_r > 0.4,

and that for Re = 582 and 715 firstly rapidly decreases as W_r/S_r < 0.3 and then increases

slowly. For MCHS-OFR, the $S_{gen}/S_{gen,0}$ for Re = 187 generally decreases with W_r/S_r as W_r/S_r >

0.5, and the ones for Re = 582 and 715 decrease with increase of W_r/S_r as W_r/S_r < 0.3 and then

increase as W_r/S_r > 0.3. With the increase of W_r/S_r from 0.125 to 1, the $S_{gen}/S_{gen,0}$ for

MCHS-AFR changes in the ranges of 0.74-0.82, 0.7-0.75, 0.71-0.74, 0.75-0.82 and 0.85-0.96

respectively for Re = 187, 316, 443, 582 and 715, and the $S_{gen}/S_{gen,0}$ for MCHS-OFR changes

in the ranges of 0.77-0.82, 0.69-0.75, 0.67-0.75, 0.7-0.81 and 0.75-0.9 respectively for Re =

187, 316, 443, 582 and 715. From Fig. 8b, it can be seen that the increase of Re results in

large decrease of $S_{gen,h}/S_{gen}$, and with the increase of Re, the MCHS-AFR shows much lower

$S_{gen,h}/S_{gen}$ than MCHS-OFR. As $Re = 187$, 316 and 443, the $S_{gen,h}/S_{gen}$ shows little variation

with increase of W_r/S_r; As $Re = 582$ and 715, the $S_{gen,h}/S_{gen}$ increase with increase of W_r/S_r as

$W_r/S_r < 0.25$, keeps almost the same in the range from 0.25 to 0.625, and drops for

MCHS-AFR but changes little for MCHS-OFR as $W_r/S_r > 0.625$. With the increase of W_r/S_r

form 0.125 to 1, the $S_{gen,h}/S_{gen}$ for MCHS-AFR changes in the ranges of 0.994-0.997,

0.961-0.977, 0.894-0.917, 0.781-0.826 and 0.638-0.689 respectively for $Re = 187$, 316, 443,

582 and 715, and the $S_{gen,h}/S_{gen}$ for MCHS-OFR changes in the ranges of 0.995-0.997,

0.969-0.984, 0.912-0.949, 0.829-0.889 and 0.731-0.805 respectively for $Re = 187$, 316, 443,

582 and 715.

Figures 9a and 9b show the effects of H_r/W_c and Re on $S_{gen}/S_{gen,0}$ and $S_{gen,h}/S_{gen}$. The

geometry of fan-shaped ribs used in these figures is $W_c = 0.1$ mm, $S_r = 0.4$ mm, $W_r = 0.1$ mm

and $H_r = 0.005$-0.025 mm. From Fig. 9a, it can be seen that the increase of H_r/W_c leads to

decrease of $S_{gen}/S_{gen,0}$ for lower Re ($Re = 187$, 316 and 443), while first decrease and then

increase for larger Re ($Re = 582$ and 715), and the turning point is earlier for larger Re and

MCHS-AFR. With the increase of H_r/W_c form 0.05 to 0.25, the $S_{gen}/S_{gen,0}$ decreases from

0.947 to 0.823, 0.925 to 0.733, 0.918 to 0.716, 0.918 to 0.719 then 0.761, and 0.921 to 0.739

then 0.956 for MCHS-AFR respectively at $Re = 187$, 316, 443, 582 and 715; from 0.957 to

0.813, 0.946 to 0.731, 0.947 to 0.699, 0.952 to 0.699, 0.958 to 0.747 for MCHS-OFR

respectively at $Re = 187$, 316, 443, 582 and 715. From Fig. 9b, it is noticed that the increases

of Re and H_r/W_c result in large decrease of $S_{gen,h}/S_{gen}$, and the decrease rate of $S_{gen,h}/S_{gen}$ with

Re increases with increase of H_r/W_c. As *Re* = 187, the MCHS-AFR shows almost the same $S_{gen,h}/S_{gen}$ with MCHS-OFR, while with the increase of *Re*, the MCHS-AFR shows much lower $S_{gen,h}/S_{gen}$ than MCHS-OFR. With the increase of H_r/W_c from 0.05 to 0.25, the $S_{gen,h}/S_{gen}$ decreases from 0.999 to 0.997, 0.994 to 0.976, 0.982 to 0.919, 0.963 to 0.825, and 0.936 to 0.691 for MCHS-AFR respectively at *Re* = 187, 316, 443, 582 and 715; from 0.999 to 0.998, 0.994 to 0.984, 0.983 to 0.949, 0.965 to 0.884, and 0.939 to 0.793 for MCHS-OFR respectively at *Re* = 187, 316, 443, 582 and 715.

Figures 10a and 10b show the effects of S_r/W_c and *Re* on $S_{gen}/S_{gen,0}$ and $S_{gen,h}/S_{gen}$. The geometry of fan-shaped ribs used in these figures is W_c = 0.1 mm, W_r = 0.1 mm, H_r = 0.025 mm and S_r = 0.2-5 mm. From Fig. 10a, it can be seen that for lower *Re* (*Re* = 187 and 316), the decrease of S_r/W_c leads to obvious decrease of $S_{gen}/S_{gen,0}$, while for higher *Re* (*Re* = 443, 582 and 715), the $S_{gen}/S_{gen,0}$ firstly decreases and then increases, and the turning point of S_r/W_c is larger for larger *Re* and MCHS-AFR. With the decrease of S_r/W_c from 50 to 2, the $S_{gen}/S_{gen,0}$ decreases from 0.971 to 0.745, 0.952 to 0.682, 0.939 to 0.709 then 0.715, 0.926 to 0.761 then 0.821, and 0.915 to 0.902 then 1.014 for MCHS-AFR respectively for *Re* = 187, 316, 443, 582 and 715; from 0.979 to 0.758, 0.936 to 0.674, 0.978 to 0.678 then 0.685, 0.937 to 0.699 then 0.762, and 0.934 to 0.739 then 0.896 for MCHS-OFR respectively for *Re* = 187, 316, 443, 582 and 715. From Fig. 10b, it can be seen that the increase of *Re* and decrease of S_r/W_c result in large decrease of $S_{gen,h}/S_{gen}$, and the decrease rate of $S_{gen,h}/S_{gen}$ with *Re* increases with decrease of S_r/W_c. With the decrease of S_r/W_c from 50 to 2, the $S_{gen,h}/S_{gen}$ decreases from 0.999 to 0.995, 0.994 to 0.958, 0.981 to 0.869, 0.959 to 0.72, and 0.929 to 0.542 for MCHS-AFR respectively for *Re* = 187, 316, 443, 582 and 715; from 0.999 to 0.996, 0.994 to 0.966, 0.981

to 0.891, 0.958 to 0.766, and 0.925 to 0.634 for MCHS-OFR respectively for Re = 187, 316,

443, 582 and 715.

4.3. Performance evaluation criterion

Figure 11 shows the effects of Re and W_r/S_r on *PEC*. The geometry of fan-shaped ribs

used in these figures is the same to Fig. 8. From Fig. 11a, it is noted that with increase of Re,

the *PEC* firstly increases and then decreases, and the maximum occurs more early for the

MCHS-AFR and larger W_r/S_r. It can be seen that with the increase of Re and W_r/S_r, the *PEC*

can be lower than 1, indicating that the performance of such heat sink is worse than the

MCHS under those conditions. From Fig. 11b, it can be seen that the W_r/S_r has more influence

on *PEC* for MCHS-OFR than MCHS-AFR, and the MCHS-OFR with W_r/S_r < 0.7 shows

better performance than MCHS-AFR. For MCHS-OFR, as Re = 187 and 316, the *PEC*

generally decrease with increase of W_r/S_r; as Re = 443, 582 and 715, the *PEC* increases as

W_r/S_r < 0.3 and decreases as W_r/S_r > 0.3. For MCHS-AFR, there is no clear tendency of *PEC*

with W_r/S_r. With the increase of W_r/S_r from 0.125 to 1, the *PEC* for MCHS-AFR changes in

the ranges of 1.01-1.12, 1.04-1.16, 1.01-1.15, 0.96-1.13 and 0.94-1.09 respectively for Re =

187, 316, 443, 582 and 715, and the *PEC* for MCHS-OFR decreases from 1.23 to 1.05, 1.37

to 1.05, 1.35 to 1.37 then 1.03, 1.28 to 1.33 then 0.99, 1.21 to 1.30 then 0.97.

Figure 12 shows the effects of Re and H_r/W_c on *PEC*. The geometry of fan-shaped ribs

used in these figures is the same to Fig. 9. From Fig. 12a, it can be seen that as H_r/W_c = 0.05,

the MCHS-AFR shows larger *PEC* than MCHS-OFR, while as H_r/W_c = 0.15 and 0.25, the

PEC shows the contrary tendency, further as H_r/W_c = 0.15, the *PEC* extremely increases with

Re. From Fig. 12b, it can be seen that for MCHS-AFR, as *Re* = 187 and 316, the *PEC* firstly

decreases, then increases and decreases again with the increase of H_r/W_c, while as *Re* = 443,

582 and 715, the *PEC* firstly increases and then decreases and the maximum occurs more

early for larger *Re*. For MCHS-OFR, the *PEC* generally increases with H_r/W_c, except the

cases as *Re* = 715 and H_r/W_c > 0.15. In general, the MCHS-AFR shows better performance

than MCHS-AFR as H_r/W_c < 0.15, while the contrary tendency as H_r/W_c > 0.15. With the

increase of H_r/W_c from 0.05 to 0.25, the *PEC* increases from 1.08 to 1.17 then 1.13, 1.09 to

1.26 then 1.11, 1.08 to 1.29 then 1.11, and 1.08 to 1.33 then 1.08, for MCHS-AFR

respectively at *Re* = 316, 443, 582 and 715; from 1.04 to 1.19, 1.06 to 1.29, 1.05 to 1.32, 1.04

to 1.33, 1.03 to 1.29 for MCHS-OFR respectively at *Re* = 187, 316, 443, 582 and 715.

Figure 13 shows the effects of *Re* and S_r/W_c on *PEC*. The geometry of fan-shaped ribs

used in these figures is the same to Fig. 10. From Fig. 13a, it can be seen that as S_r/W_c = 20

and 10, the *PEC* increases with *Re*; as S_r/W_c = 5 and 2.5, the *PEC* firstly increases and then

decreases with increase of *Re*. From Fig. 13b, it is noted that with decrease of S_r/W_c, the *PEC*

firstly increases and then decrease for both MCHS-AFR and MCHS-OFR; The maximums of

PEC for MCHS-AFR usually occur at a larger S_r/W_c in the range of from 4 to 12.5; The

maximums of *PEC* for MCHS-OFR are much higher than MCHS-AFR. With the decrease of

S_r/W_c from 50 to 2, the *PEC* changes in the range of 0.99-1.07, 1.02-1.14, 1.03-1.14,

0.99-1.17, and 0.95-1.16 for MCHS-AFR respectively for *Re* = 187, 316, 443, 582 and 715;

0.97-1.23, 0.99-1.34, 0.99-1.32, 1.01-1.32 and 1.02-1.33 for MCHS-OFR respectively for *Re*

= 187, 316, 443, 582 and 715. From Figs. 11, 12 and 13, it also can be found that the *PEC* is

an applicable and flexible design parameter to present the comprehensive thermal

5. Conclusions

In the third part of the three-part study, the relationship between thermal resistance and pumping power, entropy generation rate and performance evaluation criteria for laminar flow in microchannel heat sinks with fan-shaped ribs on sidewalls have been studied. With respect to the smooth baseline channels, the new conclusions drawn in this paper are summarized as follows:

(1). The geometric parameters of fan-shaped ribs have a significant influence on the performance of such microchannel heat sinks. With the increase of the rib's height, the microchannel heat sinks with offset fan-shaped ribs gradually perform better than the ones with aligned fan-shaped ribs. With the increase of the rib's spacing, the comprehensive performance firstly improved and then gradually deteriorates. The rib's width has more influence on MCHS-OFR than MCHS-AFR. The large rib's width can result in the deterioration of performance.

(2). For the microchannel heat sink with large rib's height and small rib's spacing, the increase of Reynolds number can lead to tremendously increase of entropy generation rate due to fluid friction, which can withdraw the decrease of entropy generation rate due to heat transfer and lead to the increase of total entropy generation rate, making the comprehensive performance worse than the smooth one.

(3). The fan-shaped ribs can lead to better comprehensive performance than MCHS. For

17

Reynolds number ranging from 187 to 715 and studied geometric parameters, the best

microchannel heat sink shows a 32% decrease in entropy generation rate and 1.33 in

performance evaluation criterion, comparing with the MCHS.

Acknowledgements

References

[1]   S. Kandlikar, S Garimella, D. Li, S. Colin, M.R. King, Heat transfer and fluid flow in minichannels and microchannels, Elsevier, 2005.

[2]   J.L. Xu, Y.H. Gan, D.C. Zhang, Microscale heat transfer enhancement using thermal boundary layer redeveloping concept, International Journal of Heat and Mass Transfer 48 (2005) 1662-1674.

[3]   J.L. Xu, Y.X. Song, W. Zhang, Numerical simulations of interrupted and conventional microchannel heat sinks, International Journal of Heat and Mass Transfer 51 (2008) 5906-5917.

[4]   L. Chai, G.D. Xia, L. Wang, Heat transfer enhancement in microchannel heat sinks with periodic expansion–constriction cross-sections, International Journal of Heat and Mass Transfer 62 (2013) 741–751.

[5]   L. Chai, G.D. Xia, M.Z. Zhou, Numerical simulation of fluid flow and heat transfer in a microchannel heat sink with offset fan-shaped reentrant cavities in sidewall, International Communications in Heat and Mass Transfer 38 (2011) 577-584.

[6]   Y.J. Cheng, Numerical simulation of stacked microchannel heat sink with mixing–enhanced passive structure, International Communications in Heat and Mass Transfer 34 (2007) 295-303.

[7]   F. Hong, P. Cheng, Three dimensional numerical analyses and optimization of offset strip–fin microchannel heat sinks, International Communications in Heat and Mass

Transfer 36 (2009) 651–656.

[8]   A.J. Foong, N. Ramesh, Laminar convective heat transfer in a microchannel with internal longitudinal fins, International Journal of Thermal Sciences 48 (2009) 1908-1913.

[9]   L. Chai, G. Xia, M. Zhou, J. Li, J. Qi, Optimum thermal design of interrupted microchannel heat sink with rectangular ribs in the transverse microchambers, Applied Thermal Engineering 51 (2013) 880-889.

[10]   S. Kandlikar, S Garimella, D. Li, S. Colin, M.R. King, Heat transfer and fluid flow in minichannels and microchannels, Elsevier, 2005.

[11]   T.H. Tsai, R. Chein, Simple model for predicting microchannel heat sink performance and optimization, Heat and Mass Transfer 48 (2012) 789-798.

[12]   D. Liu, S.V. Garimella, Analysis and optimization of the thermal performance of microchannel heat sinks, International Journal of Numerical Methods for Heat & Fluid Flow 15 (2005) 7-26.

[13]   S. Vishal, D. Liu, S.V. Garimella, Analysis of pumping requirements for microchannel cooling systems, ASME 2003 International Electronic Packaging Technical Conference and Exhibition. American Society of Mechanical Engineers, 2003.

[14]   S.V. Garimella, S. Vishal, Single-phase flow and heat transport and pumping considerations in microchannel heat sinks, Heat transfer engineering 25 (2004) 15-25.

[15]   L. Gosselin, A. Bejan, Tree networks for minimal pumping power, International Journal of Thermal Sciences 44 (2005) 53-63.

[16] P. Canhoto, A.H. Reis, Optimization of forced convection heat sinks with pumping power requirements, International Journal of Heat and Mass Transfer 54 (2011) 1441-1447.

[17] G. Xie, H. Shen, C.C. Wang, Parametric study on thermal performance of microchannel heat sinks with internal vertical Y-shaped bifurcations, International Journal of Heat and Mass Transfer 90 (2015) 948-958.

[18] M. Famouri, K. Hooman, F. Hooman, Effects of thermal boundary condition, fin size, spacing, tip clearance, and material on pressure drop, heat transfer, and entropy generation optimization for forced convection from a variable-height shrouded fin array, Heat Transfer Research 40 (2009).

[19] Z. Shi, T. Dong, Entropy generation and optimization of laminar convective heat transfer and fluid flow in a microchannel with staggered arrays of pin fin structure with tip clearance, Energy Conversion and Management 94 (2015) 493-504.

[20] P. Promvonge, S. Sripattanapipat, S. Kwankaomeng, Laminar periodic flow and heat transfer in square channel with 45° inline baffles on two opposite walls, International Journal of Thermal Sciences 49 (2010) 963–975.

[21] G.D. Xia, L. Chai, M.Z. Zhou, Effects of structural parameters on fluid flow and heat transfer in a microchannel with aligned fan-shaped reentrant cavities, International Journal of Thermal Sciences 50 (2011) 411–419.

[22] G.D. Xia, L. Chai, H.Y. Wang, Optimum thermal design of microchannel heat sink with triangular reentrant cavities, Applied Thermal Engineering 31 (2011) 1208–1219.

[23] J. Zhang, Y. Zhao, Y. Diao, Y. Zhang, An experimental study on fluid flow and heat

transfer in a multiport minichannel flat tube with micro-fin structures, International Journal of Heat and Mass Transfer 84 (2015) 511-520.

[24]   F.P. Incropera, Liquid cooling of electronic devices by single-phase convection, Wiley, 1999.

[25]   L. Chai, G.D. Xia, H.S. Wang, Numerical study of laminar flow and heat transfer in microchannel heat sink with offset ribs on sidewalls, Applied Thermal Engineering 92 (2016) 32–41.

[26]   P. Loosen, Cooling and packaging of high-power diode lasers, High-Power Diode Lasers, Springer Berlin Heidelberg 78 (2000) 289-301.

[27]   W.A. Khan, M.M. Yovanovich, J.R. Culham, Optimization of microchannel heat sinks using entropy generation minimization method. In Semiconductor Thermal Measurement and Management Symposium, 22nd IEEE Twenty-Second Annual IEEE, 2006, 78-86.

[28]   R.L. Webb, Performance evaluation criteria for use of enhanced heat transfer surfaces in heat exchanger design, International Journal of Heat and Mass Transfer 24 (1981) 715-726.

Nomenclature

A	Area, $\mathrm{m^2}$
c_p	Specific heat, $\mathrm{J \cdot kg^{-1}\ K^{-1}}$
D_h	Hydraulic diameter, m
$\bar{f}$	Average friction factor
$\bar{f}_0$	Average friction factor for the smooth microchannel
h	Heat transfer coefficient, $\mathrm{W \cdot m^{-2}\ \cdot K^{-1}}$
$\bar{h}$	Average heat transfer coefficient, $\mathrm{W \cdot m^{-2}\ \cdot K^{-1}}$
$\bar{h}_0$	Average heat transfer coefficient for the smooth microchannel, $\mathrm{W \cdot m^{-2}\ \cdot K^{-1}}$
H	Height, m
k	Thermal conductivity, $\mathrm{W \cdot m^{-1}\ \cdot K^{-1}}$
L	Length, m
$\overset{\mathrm{g}}{m}$	Fluid mass flow rate, $\mathrm{kg \cdot s^{-1}}$
Nu	Nusselt number
$\overline{Nu}$	Average Nusselt number
$\overline{Nu}_0$	Average Nusselt number for the smooth microchannel heat sink
p	Pressure, Pa
Δp	Pressure drop, Pa
PEC	Performance evaluation criteria
P_p	Pumping power, W
q	Heat flux, $\mathrm{W \cdot m^{-2}}$

Q	Heat transfer rate, W
Re	Reynolds number
R_{th}	Total thermal resistance, $K \cdot W^{-1}$
S_{gen}	Entropy generation rate, $W \cdot K^{-1}$
$S_{gen,h}$	Entropy generation rate due to heat transfer, $W \cdot K^{-1}$
$S_{gen,f}$	Entropy generation rate due to fluid friction, $W \cdot K^{-1}$
T	Temperature, K
$\bar{T}$	Average temperature, K
u	Velocity, $m \cdot s^{-1}$
$\bar{u}$	Average velocity, $m \cdot s^{-1}$
$\overset{g}{V}$	Volume flow rate, $m^3 \cdot s^{-1}$
x,y,z	Three coordinates shown in Fig. 1, m

Greek letters

ρ	Density, $kg \cdot m^{-3}$
μ	Dynamic viscosity, $Pa \cdot s$

Subscripts

a	Ambient
c	Cross section
in	Inlet
f	Fluid
out	Outlet
pp	Pumping power

r	Rib
s	Silicon
w	Heat sink base

Figure captions

Fig. 1   Microchannel heat sinks with fan-shaped ribs on sidewalls. (a) Computational domain. (b) Geometric parameters of fan-shaped ribs.

Fig. 2   Eeffect of W_r/S_r on the relationship between R_{th} and P_p (W_c = 0.1 mm, H_r = 0.025 mm and S_r = 0.4 mm).

Fig. 3   Eeffect of H_r/W_c on the relationship between R_{th} and P_p (W_c = 0.1 mm, S_r = 0.4 mm and W_r = 0.1 mm).

Fig. 4   Eeffect of S_r/W_c on the relationship between R_{th} and P_p (W_c = 0.1 mm, W_r = 0.1 mm and H_r = 0.025 mm).

Fig. 5   Effects of W_r/S_r on S_{gen}, $S_{gen,h}$ and $S_{gen,f}$ (W_c = 0.1 mm, H_r = 0.025 mm and S_r = 0.4 mm). (a) S_{gen} versus Re, (b) $S_{gen,h}$ versus Re and (c) $S_{gen,f}$ versus Re.

Fig. 6   Effects of H_r/W_c on S_{gen}, $S_{gen,h}$ and $S_{gen,f}$ (W_c = 0.1 mm, S_r = 0.4 mm and W_r = 0.1 mm). (a) S_{gen} versus Re, (b) $S_{gen,h}$ versus Re and (c) $S_{gen,f}$ versus Re.

Fig. 7   Effects of S_r/W_c on S_{gen}, $S_{gen,h}$ and $S_{gen,f}$ (W_c = 0.1 mm, W_r = 0.1 mm and H_r = 0.025 mm). (a) S_{gen} versus Re, (b) $S_{gen,h}$ versus Re and (c) $S_{gen,f}$ versus Re.

Fig. 8   Effects of W_r/S_r on $S_{gen}/S_{gen,0}$ and $S_{gen,h}/S_{gen}$ (W_c = 0.1 mm, H_r = 0.025 mm and S_r = 0.4 mm). (a) $S_{gen}/S_{gen,0}$ versus W_r/S_r and (b) $S_{gen,h}/S_{gen}$ versus W_r/S_r.

Fig. 9   Effects of H_r/W_c on $S_{gen}/S_{gen,0}$ and $S_{gen,h}/S_{gen}$ (W_c = 0.1 mm, S_r = 0.4 mm and W_r = 0.1 mm). (a) $S_{gen}/S_{gen,0}$ versus H_r/W_c and (b) $S_{gen,h}/S_{gen}$ versus H_r/W_c.

Fig. 10   Effects of S_r/W_c on $S_{gen}/S_{gen,0}$ and $S_{gen,h}/S_{gen}$ (W_c = 0.1 mm, W_r = 0.1 mm and H_r = 0.025 mm). (a) $S_{gen}/S_{gen,0}$ versus S_r/W_c and (b) $S_{gen,h}/S_{gen}$ versus S_r/W_c.

Fig. 11   Effects of W_r/S_r on PEC ($W_c = 0.1$ mm, $H_r = 0.025$ mm and $S_r = 0.4$ mm). (a) PEC versus Re and (b) PEC versus W_r/S_r.

Fig. 12   Effects of H_r/W_c on PEC ($W_c = 0.1$ mm, $S_r = 0.4$ mm and $W_r = 0.1$ mm). (a) PEC versus Re and (b) PEC versus H_r/W_c.

Fig. 13   Effects of S_r/W_c on PEC ($W_c = 0.1$ mm, $W_r = 0.1$ mm and $H_r = 0.025$ mm). (a) PEC versus Re and (b) PEC versus S_r/W_c.

Fig.1

(a)
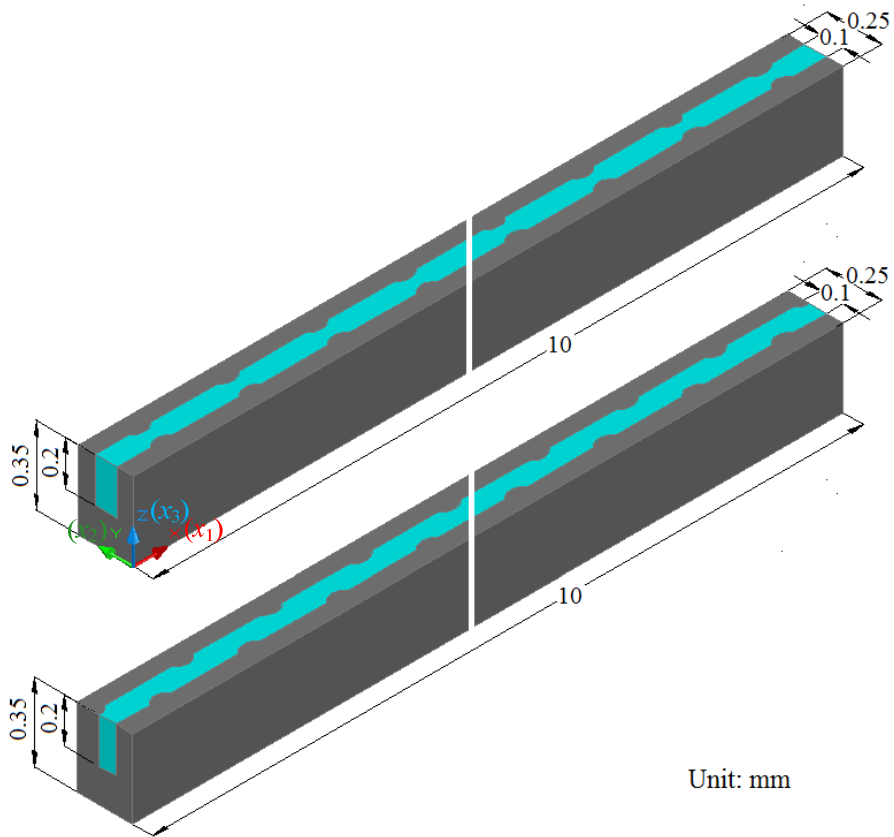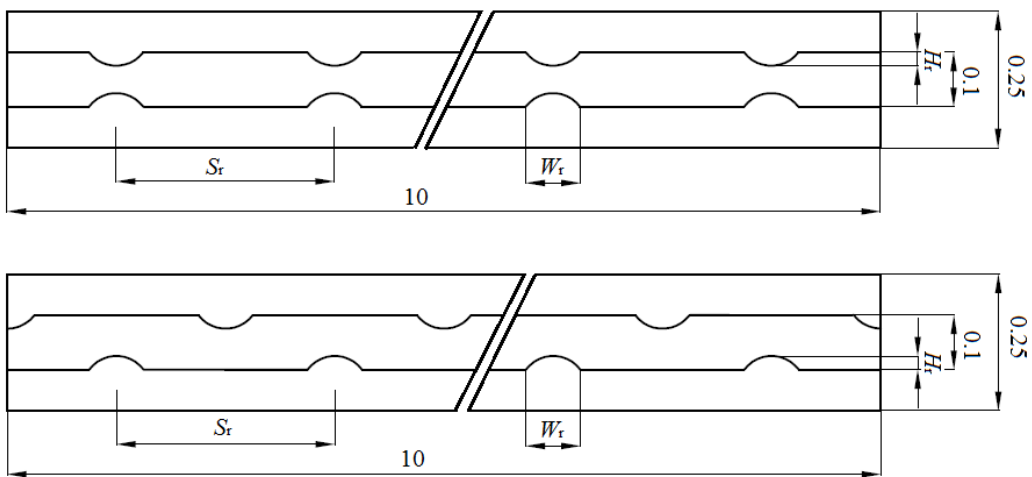
(b)

Fig.2
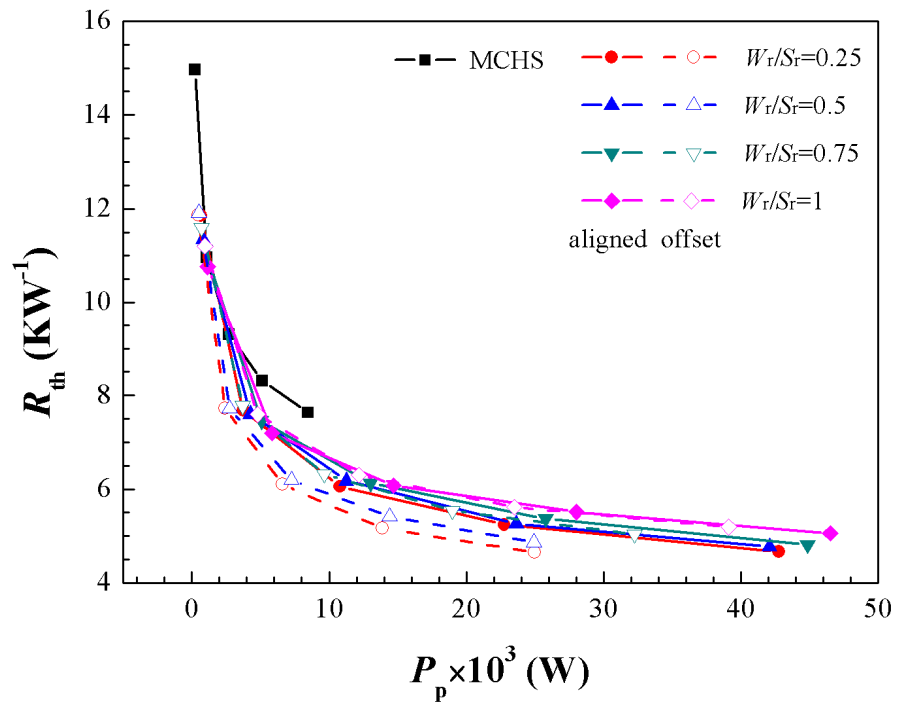
Fig.3
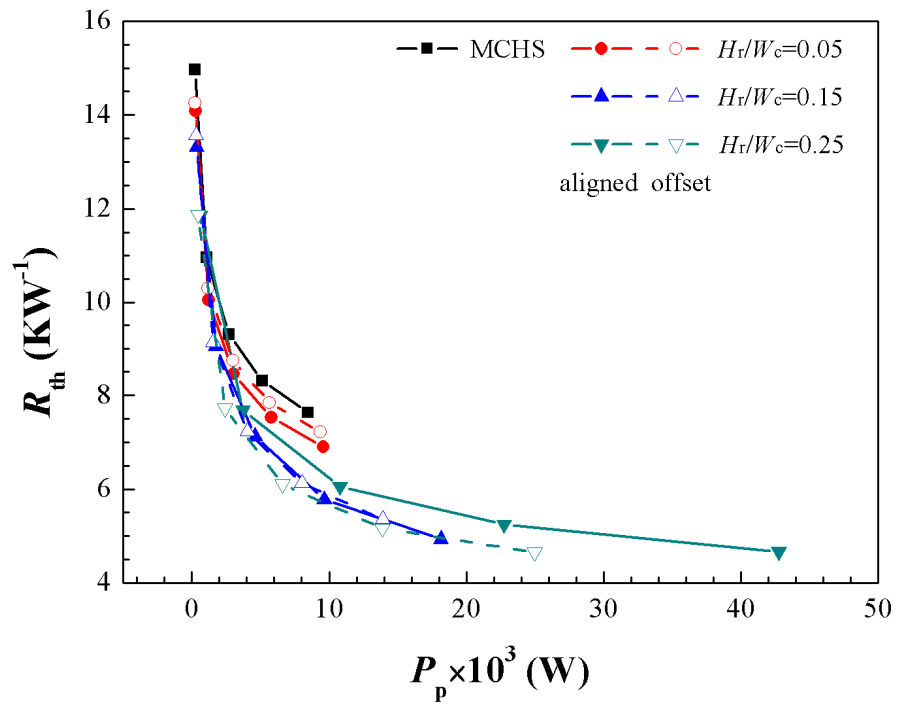
Fig.4
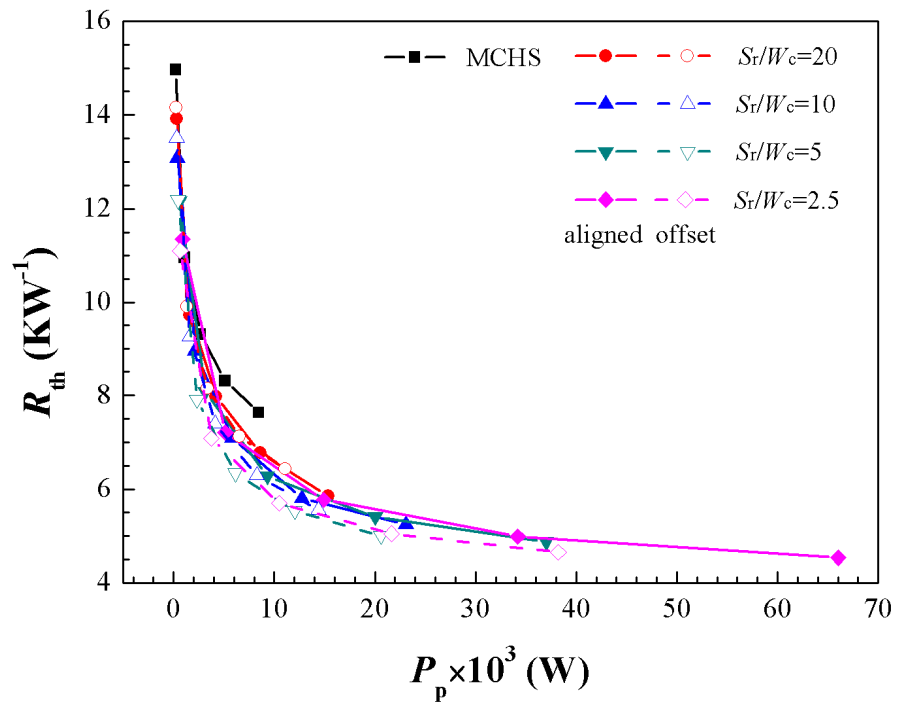
Fig.5
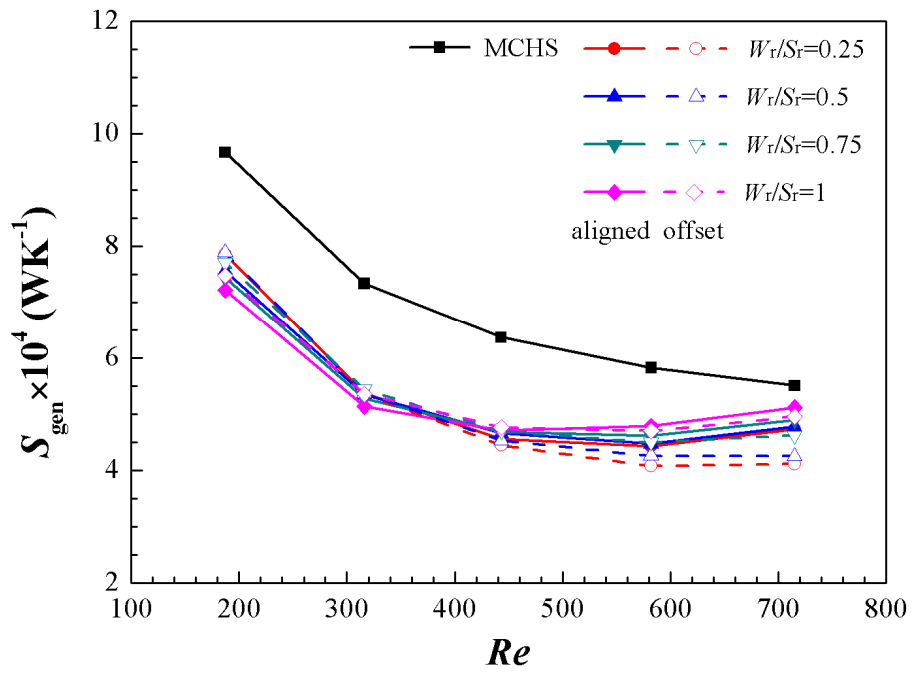
(a)
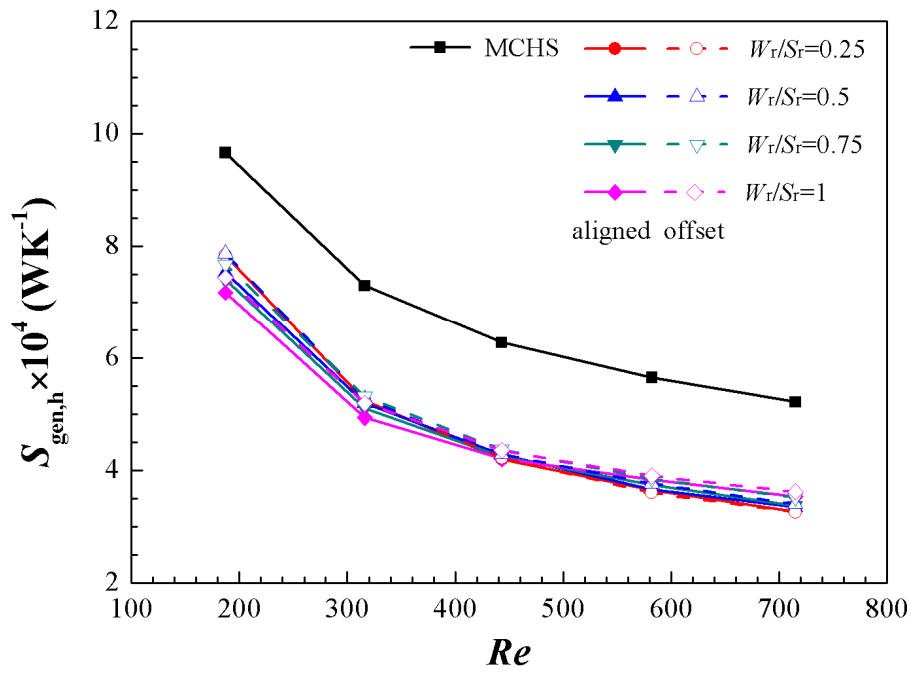
(b)
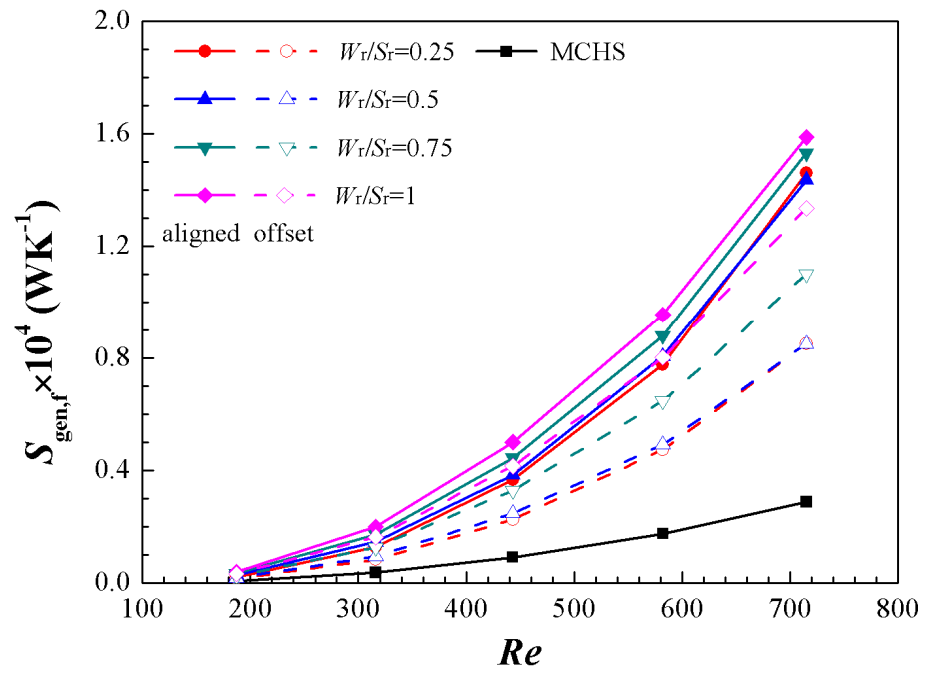
(c)

Fig.6
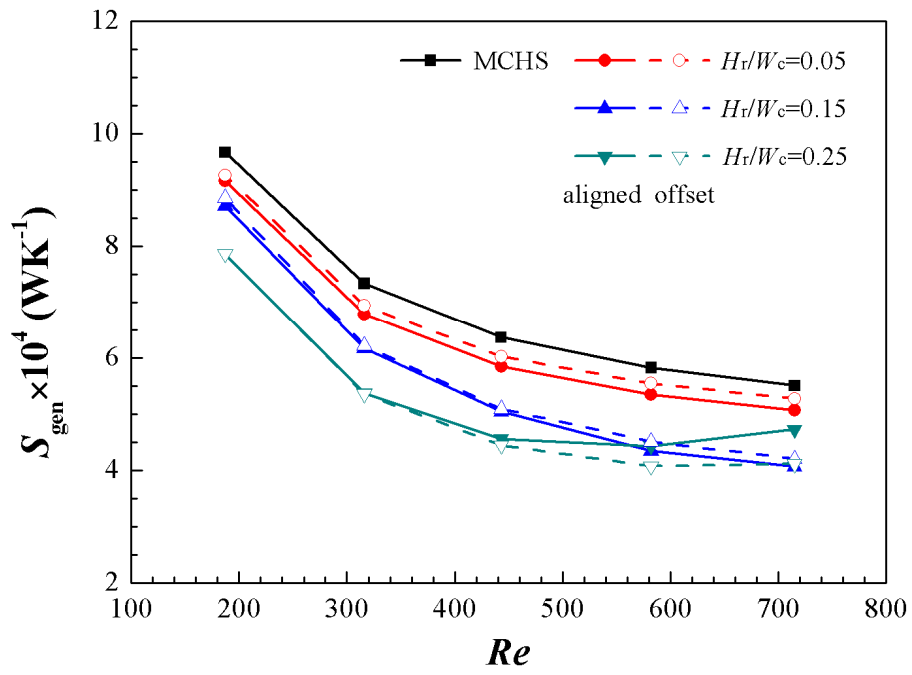
(a)
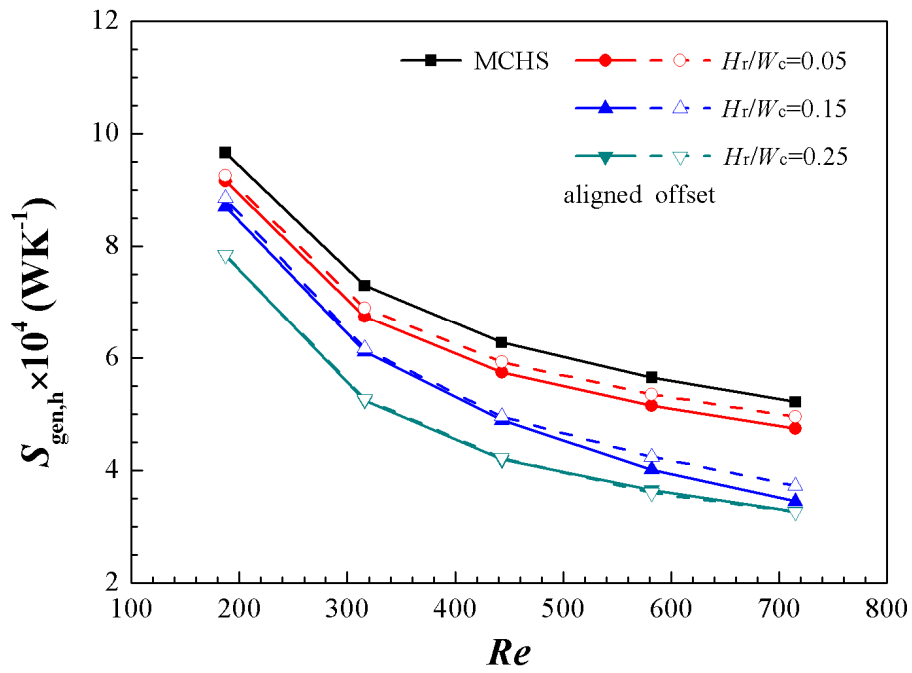
(b)
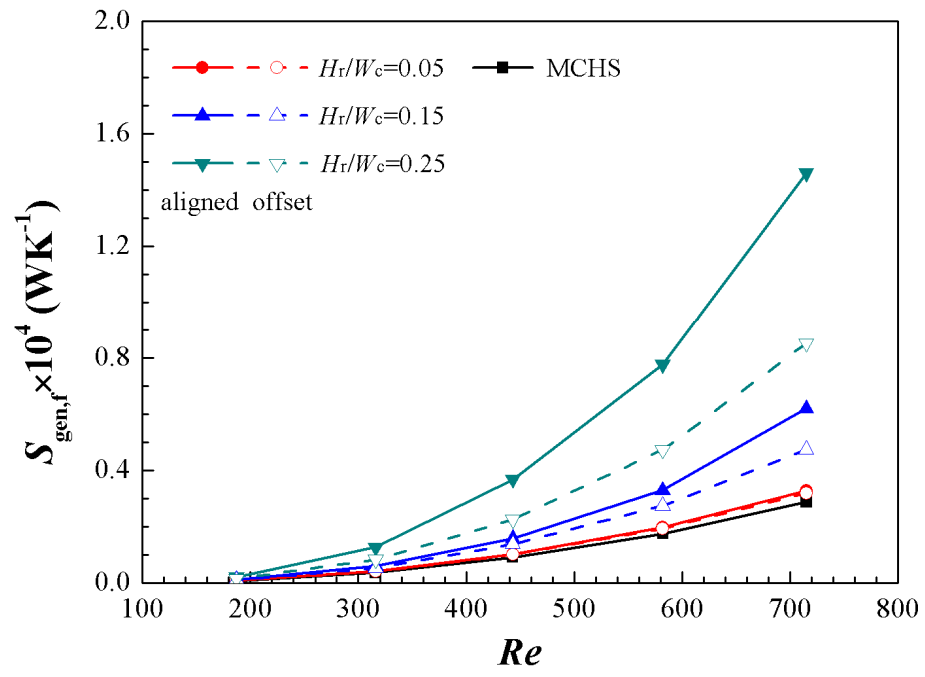
(c)

Fig.7

(a)

(b)
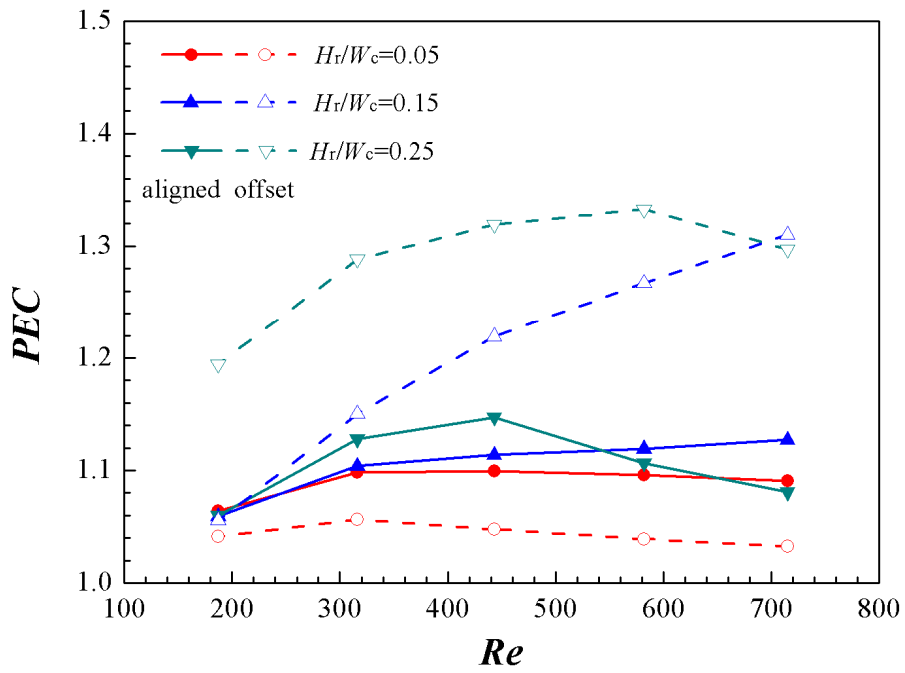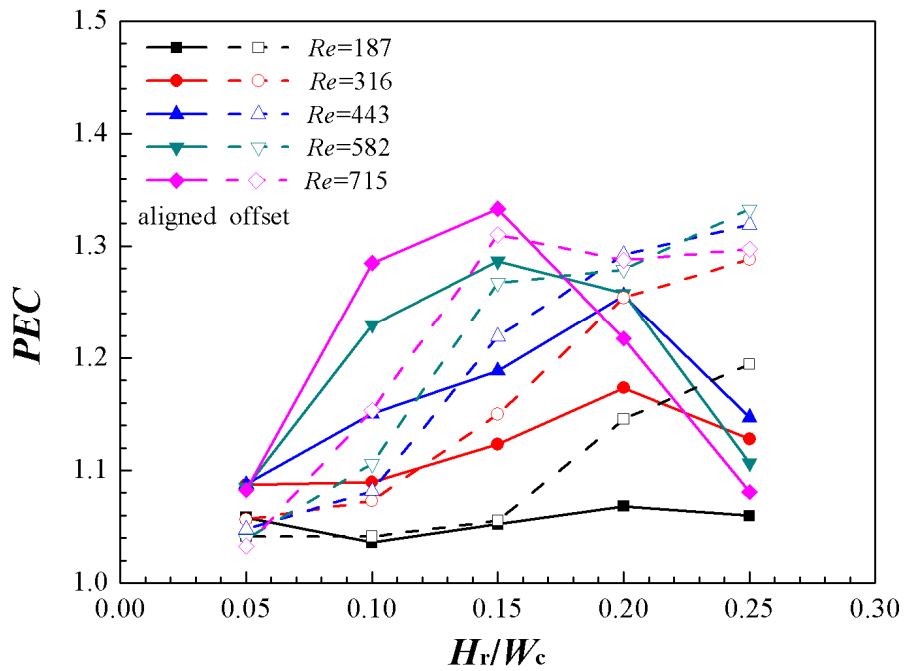
(c)

Fig.8

(a)

(b)

Fig.9

(a)

(b)

40
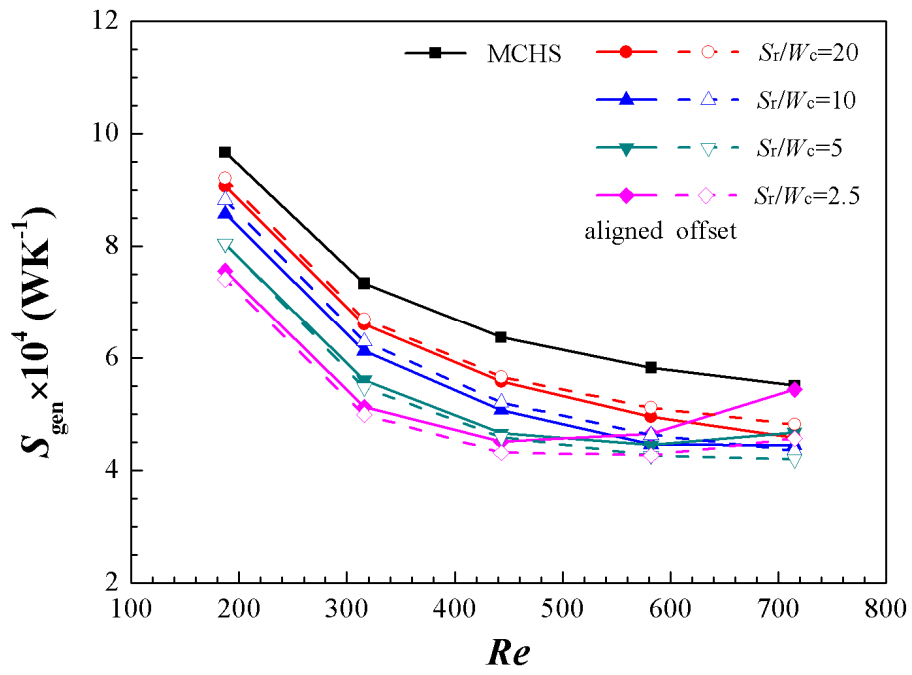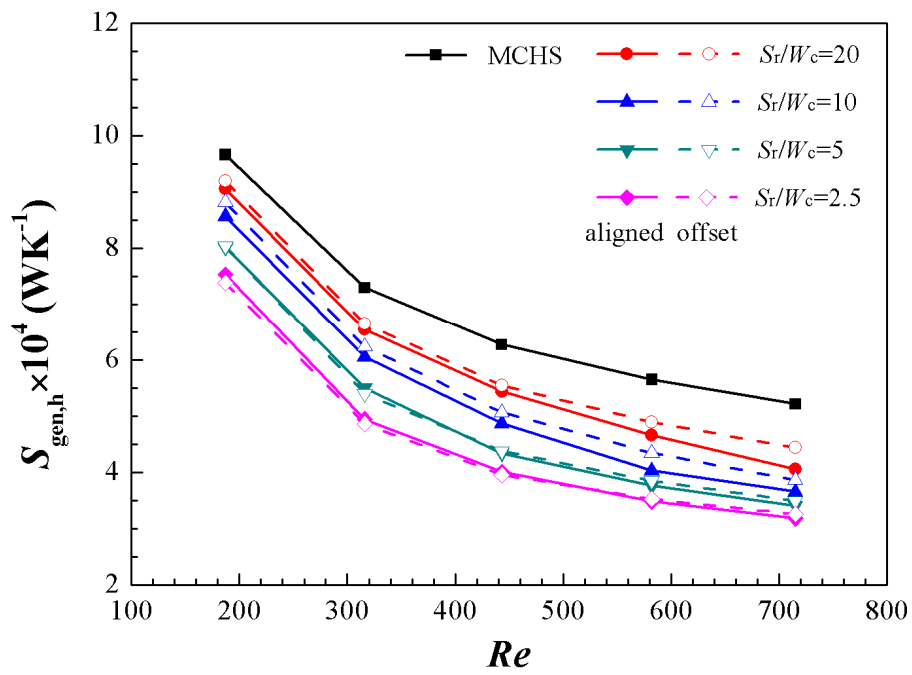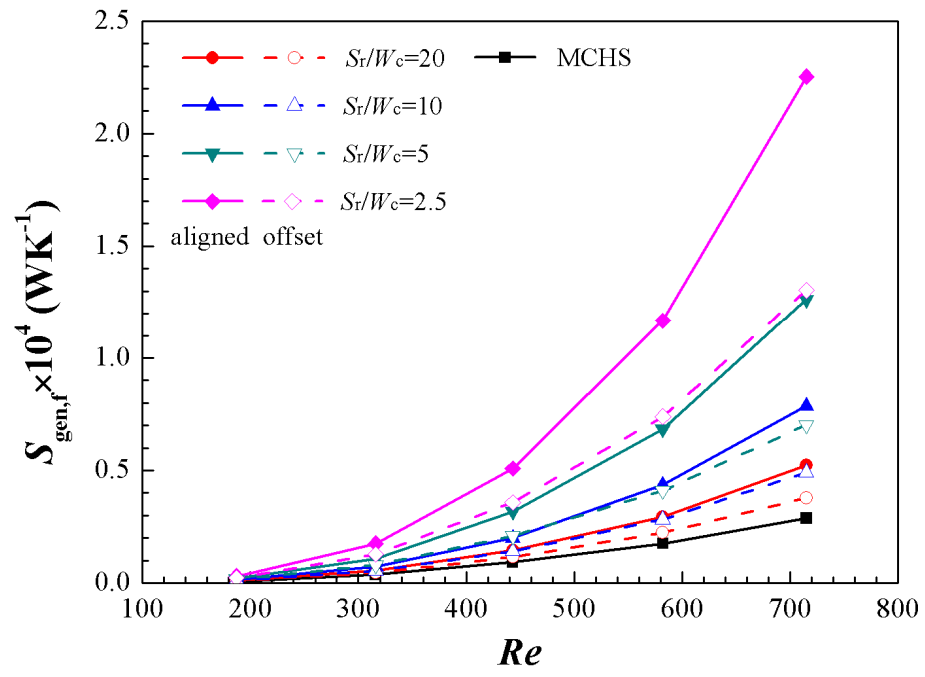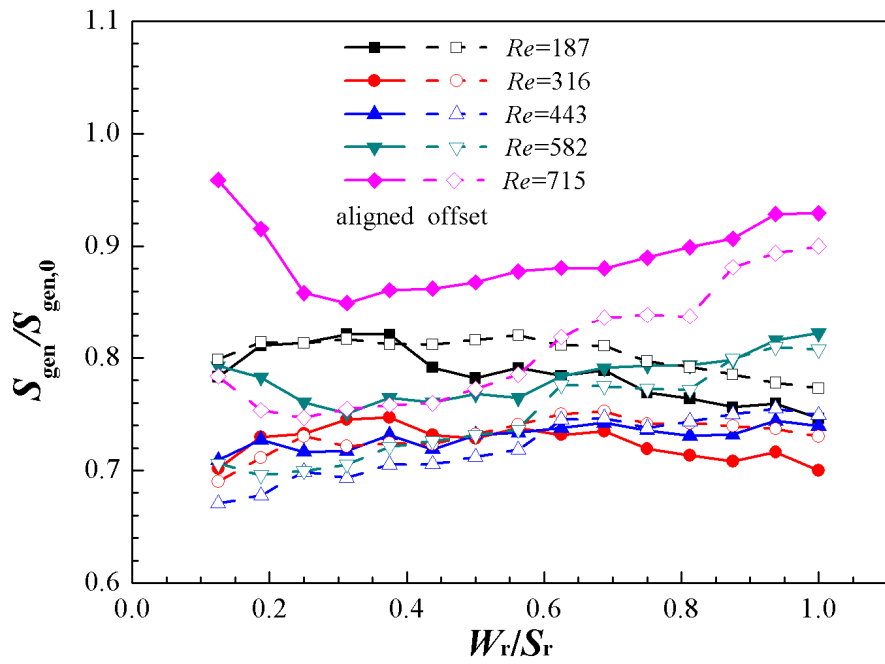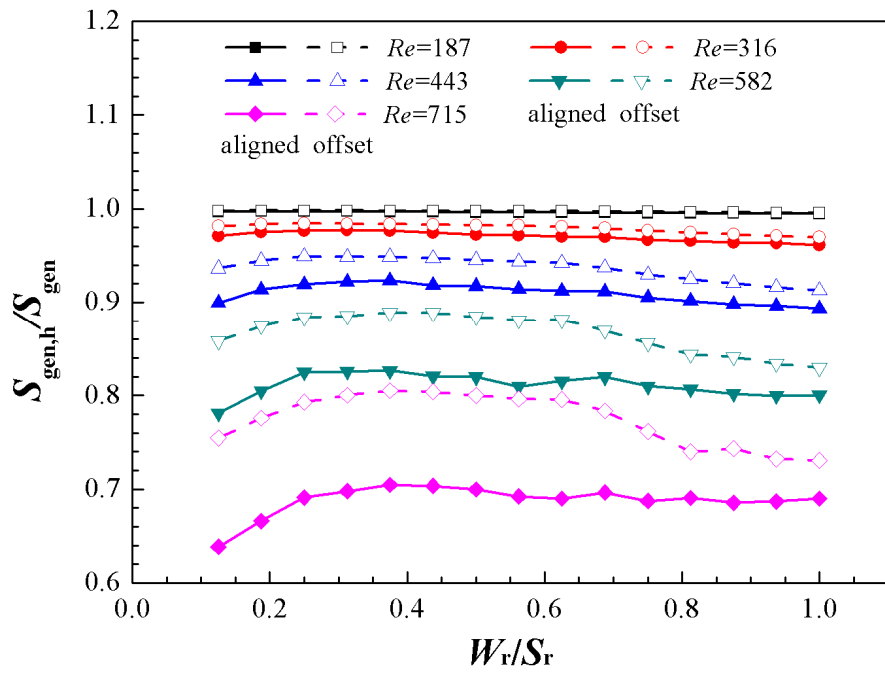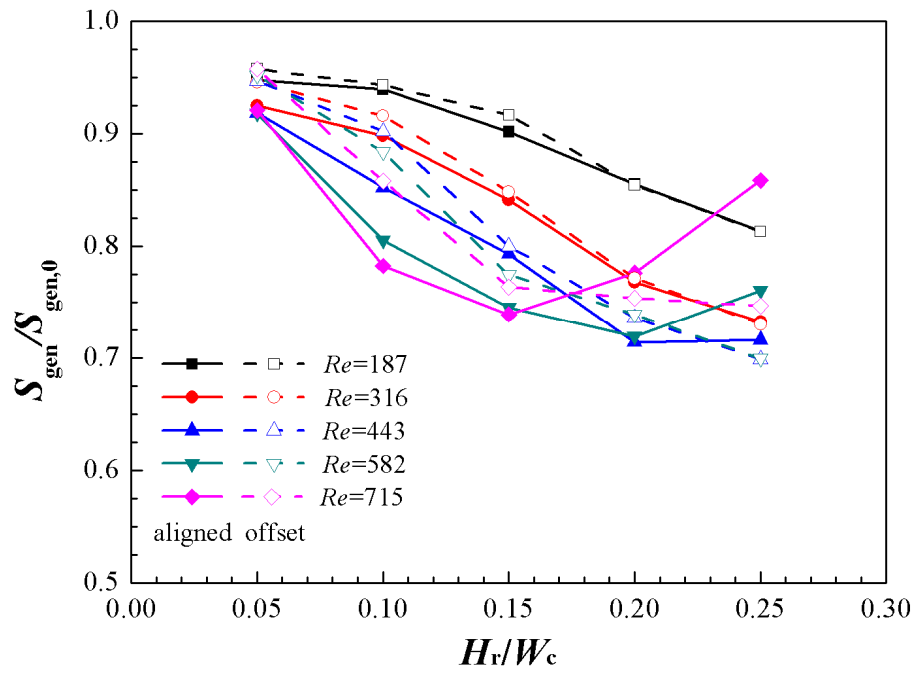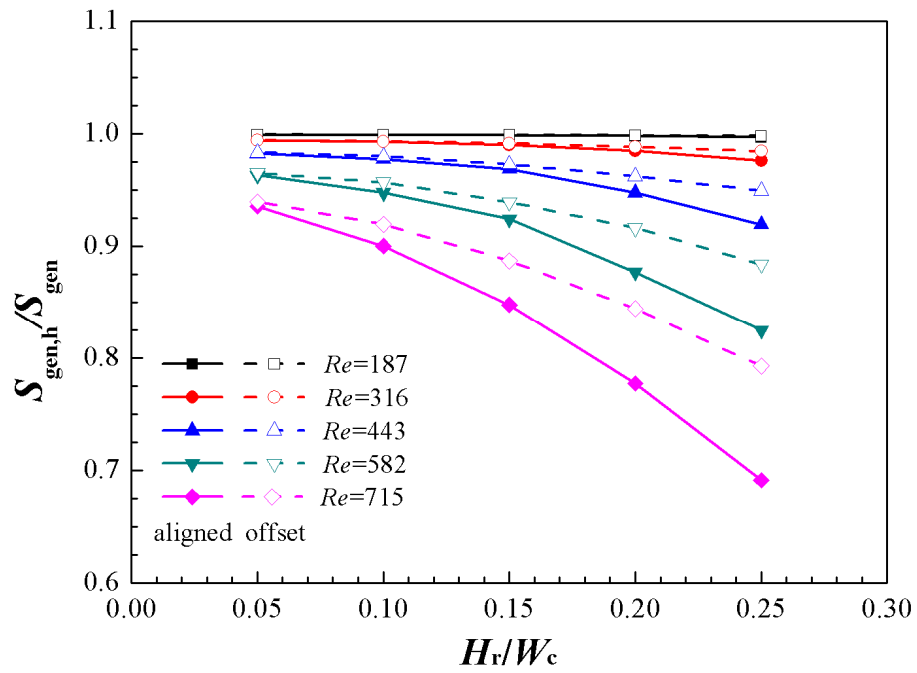
Fig.10

(a)

(b)

Fig.11

(a)

(b)

Fig.12

(a)

(b)

43

Fig.13

(a)

(b)

44